Human influence has intensified extreme precipitation in North America

Megan C. Kirchmeier-Young[a,1] and Xuebin Zhang[a]

[a]Climate Research Division, Environment and Climate Change Canada, Toronto, ONT M3H 5T4, Canada

Edited by Susan Solomon, Massachusetts Institute of Technology, Cambridge, MA, and approved April 20, 2020 (received for review December 9, 2019)

Precipitation extremes have implications for many facets of both the human and natural systems, predominantly through flooding events. Observations have demonstrated increasing trends in extreme precipitation in North America, and models and theory consistently suggest continued increases with future warming. Here, we address the question of whether observed changes in annual maximum 1- and 5-d precipitation can be attributed to human influence on the climate. Although attribution has been demonstrated for global and hemispheric scales, there are few results for continental and subcontinental scales. We utilize three large ensembles, including simulations from both a fully coupled Earth system model and a regional climate model. We use two different attribution approaches and find many qualitatively consistent results across different methods, different models, and different regional scales. We conclude that external forcing, dominated by human influence, has contributed to the increase in frequency and intensity of regional precipitation extremes in North America. If human emissions continue to increase, North America will see further increases in these extremes.

extreme precipitation | attribution | regional climate change

Recent years have seen numerous flooding and rainfall-related extreme events in North America, totaling billions of dollars in damages (1, 2). It is important to understand the drivers of these high-impact events. Observations show that extreme precipitation has increased over North America (3). Additionally, event attribution studies have identified an increased probability of some individual extreme precipitation events in this region due to anthropogenic influence (4, 5), including hurricane-induced rainfall (6). However, a current gap in our understanding is the role human influence has played in the intensification of annual maximum precipitation (referred to as extreme precipitation herein) in North America, particularly at impact-relevant scales. Here, we show robust detection and attribution results for the intensification of extreme precipitation at continental and subcontinental scales in North America.

We evaluate whether human influence has affected extreme precipitation, using two methods. The first method compares the time/space evolution to evaluate the presence of a signal and the consistency of the observations with the modeled response to external forcing. There is evidence of an anthropogenic influence on mean precipitation at global (7–9) and hemispheric (10) scales. For extreme precipitation, an anthropogenic influence has been detected and attributed for changes in the annual maxima over Northern Hemisphere land areas (11, 12). Extreme precipitation time series often exhibit small signals and high variability, especially at smaller scales, and this has hampered consistent continental or smaller-scale regional attribution (13). Using model simulations of historical and future climate change, Martel et al. (14) demonstrated that, for many regions, a significant trend in extreme precipitation cannot be distinguished from natural variability until after the mid-21st century, but is identifiable earlier than for total precipitation.

The second method is based on event attribution, which determines how individual or combined external forcings have changed the likelihood of extreme events. An increase in likelihood due to anthropogenic influence has been identified for some specific extreme events (e.g., refs. 4, 5, 15, and 16), but not for others (e.g., refs. 17–19). In general, an attributable change in the likelihood of extreme precipitation events defined over larger spatial scales and longer time periods can be found earlier (20). Fischer and Knutti (21) note that anthropogenic forcing has increased the likelihood of heavy precipitation events on a global scale at current warming levels, with further increases at higher levels of warming. When presented together, the results based on the two different attribution methods provide a more complete picture of anthropogenic influence on past and future extremes.

To understand the causes of observed changes in extreme precipitation, we utilize three large ensembles. Large initial condition ensembles produce many realizations of a single model's response to a particular forcing, by making very small changes to the initial conditions from which each simulation begins. These ensembles can provide better estimates of an individual model's internal variability and response to external forcing (22, 23) and facilitate the explicit consideration of stochastic uncertainty in attribution results. Large sample sizes are needed for event attribution in order to obtain reliable estimates of the probabilities of rare events. Large ensembles have been used for many event attribution studies (see a summary in ref. 24), including atmosphere-only ensembles like weather@home (25) designed for such assessments. Despite their benefits for detection and attribution of the spatiotemporal evolution, fully coupled single-model large ensembles remain underutilized. A comparison of attribution results from multiple large ensembles as in refs. 26 and 27 can provide new insights or improve robustness of the conclusions.

Here, we use a unique pair of large ensembles, where a 50-member large ensemble of a fully coupled Earth system model

Significance

Extreme precipitation is relevant to many interests, and observations show an increasing trend that is expected to continue under future projections. Although previous work has identified an anthropogenic influence on extreme precipitation at hemispheric scales, this study finds robust results for a continental scale. We establish that anthropogenic climate change has contributed to the intensification of continental and regional extreme precipitation. Furthermore, we also show that the anthropogenic influence on North American regional precipitation will lead to more frequent and intense precipitation extremes in the future.

Author contributions: M.C.K.-Y. and X.Z. designed research; M.C.K.-Y. performed research; M.C.K.-Y. analyzed data; and M.C.K.-Y. and X.Z. wrote the paper.

The authors declare no competing interest.

This article is a PNAS Direct Submission.

[1]To whom correspondence may be addressed. Email: megan.kirchmeier-young@canada.ca.

This article contains supporting information online at https://www.pnas.org/lookup/suppl/doi:10.1073/pnas.1921628117/-/DCSupplemental.

First published June 1, 2020.

(Canadian Earth System Model, version 2 [CanESM2]) (28) was used to drive a regional large ensemble (Canadian Regional Climate Model, version 4 [CanRCM4]) in a coordinated modeling approach (29). In addition, we also include the 40-member large ensemble performed with the widely used Community Earth System Model (CESM1) (30). All three ensembles use historical forcing through 2005, followed by Representative Concentration Pathway 8.5 (RCP8.5) forcing through 2100 (hereafter, ALL). In addition, CanESM2 also contains 50 members with natural-only forcing (NAT).

Many of the physical processes that produce extreme rainfall occur at spatial scales smaller than those that can be reliably simulated by available models. Local-scale events are not well captured. Despite these caveats, model-simulated precipitation is useful for assessing long-term trends and for studying physical processes at subcontinental and larger scales.

Observed and Projected Changes

We focus on the annual maxima of 1-d (Rx1day) and 5-d (Rx5day) rainfall. Rx1day is important for flash floods as well as infrastructure design. Rx5day is relevant to large-scale river flooding. Both metrics are commonly used to assess extreme precipitation and are available from the HadEX2 observational dataset (31). Before calculating regional averages, annual maxima were standardized locally by converting to a probability index (PI) as in refs. 11 and 12 based on quantiles of a generalized extreme value (GEV) distribution (see *Materials and Methods*). Larger PIs correspond to larger precipitation amounts at a given location. Spatial averages calculated from these standardized values are less sensitive to results from individual locations. The region-average PI is an average of the probability of local annual maxima.

Several spatial scales are considered (Fig. 1*A*). We first analyze a continental average for areas with suitable observational coverage (southern Canada and the United States). Next, North America is divided into three zonal bands with near-equal distribution of grid boxes. The domain also is divided into three meridional bands. The intersection of these zonal and meridional bands further divides the continent into nine smaller regions. PI values from each model were remapped to the HadEX2 grid before regional averages were calculated.

Time series of the PI for Rx1day averaged over North America and selected regions are displayed in Fig. 1 for the observations and each of three large ensembles. Additional regions are shown in *SI Appendix*, Fig. S1. For the North America mean, all models and the observations show an increase in Rx1day over the common period (1961–2010). The trend is largest in HadEX2 (5.47% over 50 y), while CanESM2 (4.25% over 50 y) and CanRCM4 (3.90% over 50 y) produce similar trends and CESM1 (1.88% over 50 y) is much smaller (*SI Appendix*, Table S1). The Canadian models show larger trends than CESM in most regions. In several (12 of 16) regions, especially central (east–west) and its subregions, HadEX2 shows trends much greater than those found in the models. In the west and central west, HadEX2 shows a decrease in extreme precipitation over this period, while all three models show increases of varying magnitude. The interannual variability in the observations can be large, but, in most cases, HadEX2 is found within the spread of each of the ensembles. Trends in Rx5day are often smaller than trends in Rx1day (*SI Appendix*, Table S1), and this difference is most notable in the observations. Future projections (using RCP8.5) show further increases through the end of the century in Rx1day and Rx5day in all regions and all models, with slightly smaller trends in CESM1.

The three large ensembles broadly show consistent intramodel spread of Rx1day and Rx5day trends (Fig. 1 and *SI Appendix*, Table S1). For all models, trends in the domain-wide mean exhibit the smallest variability between ensemble members. Larger variability is seen for the smaller regions, especially the drier regions where even small changes in precipitation may be

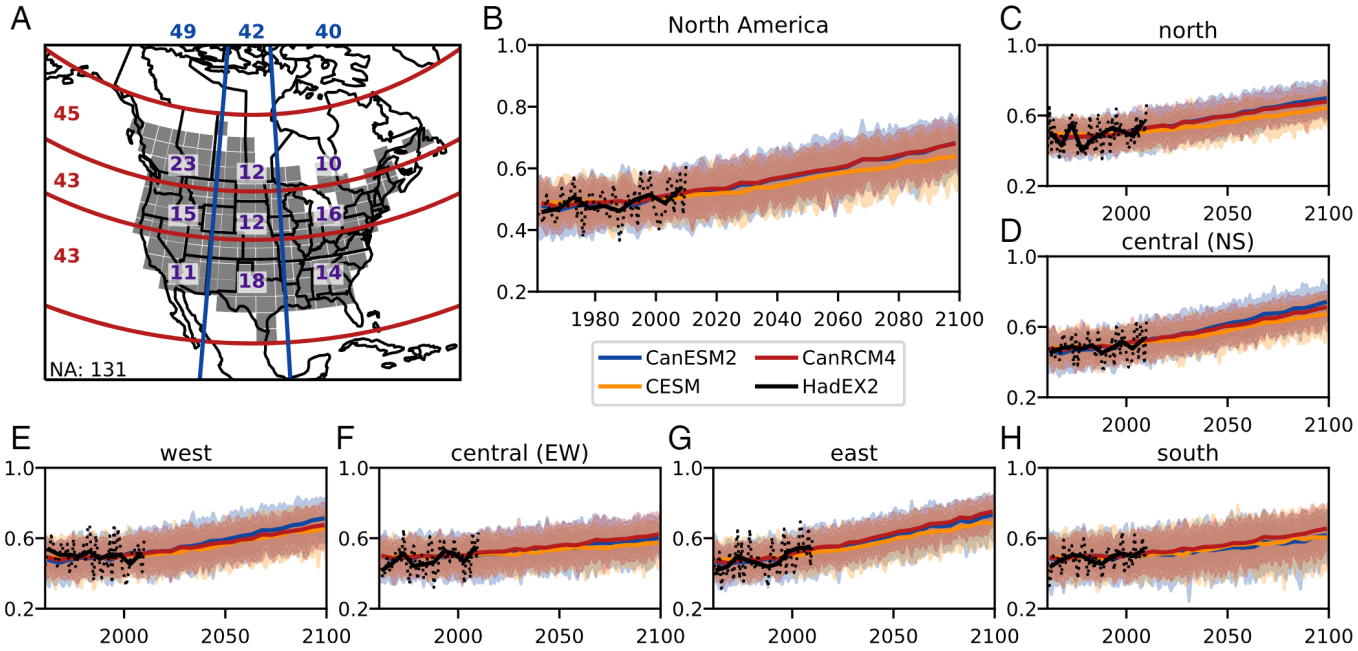

Fig. 1. Defined North American regions used herein (*A*). Blue lines separate into three east–west bands and red lines separate into three north–south bands with near-equal distribution of grid boxes. Combining gives nine regions across the domain. The gray shading shows the data mask from HadEX2 for grid boxes with coverage for more than 75% of years, and white lines show the 2.5° × 3.75° grid. Values printed in each region indicate the number of grid boxes. Time series of Rx1day PI for North America (*B*), the three north–south (NS) regions (*C*, *D*, and *H*) and three east–west (EW) regions (*E*, *F*, and *G*). Smaller regions can be found in *SI Appendix*, Fig. S1. CanESM2 is shown in blue, CanRCM4 in red, and CESM1 in orange, with the observations from HadEX2 shown in black (5-y means in solid line and annual values in dotted line). A common grid and data mask are used for each dataset. For the models, the spread indicates the 5th to 95th percentile range across the ensemble, and the bold line is 5-y means from the ensemble mean.

reflected as large changes in the PI. The ratio of the ensemble trend to the spread of trends across members is smaller for CESM1 compared to the Canadian models, due to similar ensemble variability but smaller trends. This ratio can be used to determine the likelihood that an individual realization has a positive trend (see *SI Appendix*, Table S1 for details). For the 48 Rx1day cases (across models and regions), 30 demonstrate likely positive trends, with 13 of those showing very likely positive trends. This supports confidence in the intensification of precipitation extremes.

Attribution of the Spatiotemporal Evolution

To analyze the spatiotemporal evolution (see *Materials and Methods*), we produce a scaling factor describing the relationship between the observations and model response to ALL forcing. A scaling factor significantly larger than 0.0 implies that an external forcing signal is detected in the observations. Note that not meeting this condition is not necessarily an indication of the absence of a signal, merely that a signal, if present, is not distinguishable from the variability over this period. A scaling factor that is also consistent with 1.0 indicates that the model response is of similar magnitude to the observations and supports the attribution of the observed spatiotemporal evolution to the combination of forcings. ALL forcing includes anthropogenic factors such as human emissions of greenhouse gases, atmospheric aerosols, stratospheric ozone, and land use changes and natural external factors such as volcanic and solar forcing. We utilize the many large ensemble realizations to provide as robust as possible estimates of the scaling factors and their uncertainties.

The scaling factors for a one-signal analysis with ALL, conducted separately for each of the three models, are shown in Fig. 2 for the 1961–2010 period. Results are shown for four cases: a temporal regression of North American mean values and also three spatiotemporal regressions (as in ref. 10). The latter concatenate information from the three east–west regions, the three north–south regions, and the nine smaller regions. Spatiotemporal regressions also provide information on the consistency of the spatial patterns between the model response and observations. For Rx1day, an ALL signal is detected for all regressions. The scaling factors for CanRCM4 and CanESM2 are consistent with 1.0 (and not 0.0), implying agreement between the models' response to ALL and the observations. Larger scaling factors for CESM1 indicate that this model's response is underestimated compared to observations, which is consistent with the previous trend analysis. All but one of the Rx1day regressions pass a residual consistency test, which indicates the regression residuals are generally consistent with internal climate variability.

The three models agree on the detection of an ALL signal in the observations for North American Rx1day, regardless of the level of spatial information (Fig. 2). However, they disagree on the magnitude of those changes. In order to understand the differences between models, we performed a perfect-model attribution test, where, one at a time, a realization was removed from the ensemble to act as the observations (*SI Appendix*, Fig. S2). For Rx1day, detection is found for 58 to 74% (CanRCM4), 64 to 92% (CanESM2), and 32.5 to 40% (CESM1) of realizations, with the range indicating the spread across the four space–time characterizations. These percentages are more than expected by chance, implying the detection results from Fig. 2 are robust. A lower perfect-model detection rate and wider CIs with CESM are consistent with smaller ratios of the ensemble mean trend to the spread of trends (*SI Appendix*, Table S1). There is a caveat that the widely used method for estimating the scaling factor CIs tends to underestimate their width (32). As such, the detection results presented may actually be less robust, although we are unable to test and fix this issue.

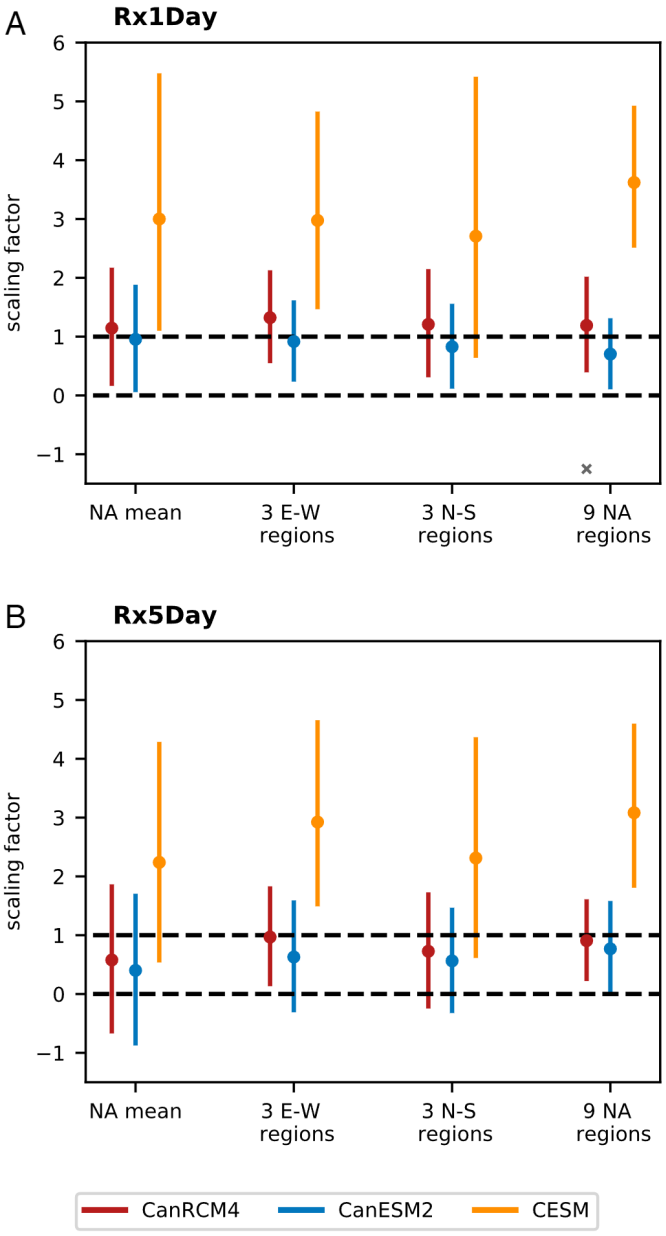

Fig. 2. Scaling factors for North American precipitation extremes from a one-signal (ALL forcing) optimal fingerprinting detection and attribution for Rx1day (*A*) and Rx5day (*B*). Results from CanRCM4 are shown in red, CanESM2 in blue, and CESM1 in orange. The first point is for a temporal regression of North American mean values, and the next three are for space–time regressions involving the concatenation of means of the designated regions (Fig. 1*A*). Error bars represent a 90% range. Gray x indicates a failure of the residual consistency test. Dashed lines are shown at 0, which indicates detection, and 1, which implies consistency with the observations.

For Rx5day, a signal is detected in all (CESM1), two (CanRCM4), and zero (CanESM2) of the North American cases. For the Canadian models, the scaling factor CIs are wider for Rx5day than for Rx1day, which contributes to the different detection results. Rx1day and Rx5day can be governed by different processes, although both annual maxima tend to occur during the same time of year. Detecting a signal more robustly with Rx1day compared to Rx5day is consistent with previous results (11, 12) at larger scales.

The CanESM2 NAT simulations show a trend in Rx1day PI of 0.44% per 50 y, which is much smaller than the ALL trend,

although the variability is similar (*SI Appendix*, Table S1). A two-signal detection and attribution analysis was conducted for CanESM2 using both ALL and NAT simulations to isolate the anthropogenic influence. An anthropogenic signal is detected and consistent with 1.0 for Rx1day in the spatiotemporal cases (*SI Appendix*, Fig. S3). The NAT signal inferred from CanESM2 is not detected in observations. This result may be partly due to masking of the observed response to volcanic forcing by internal variability, such as El Niño–Southern Oscillation (33, 34). While internal variability is largely removed in the signal when averaging across a large ensemble, its influence will still be present in the observed series. Additionally, the use of 5-y means will damp the effect of volcanic forcing in both observations and the model response. Regardless, human influence can be separated in the presence of natural external forcing. This provides a clear indication that human influence has intensified extreme precipitation in North America.

Temporal regressions for individual regions yield more uncertainty and weaker consistency with the observations (Fig. 3 for Rx1day) than was seen for spatiotemporal regressions for all of North America. There are, however, several exceptions. For example, the east exhibits the strongest positive trends and shows narrow CIs, detection in all three models, and attribution in CanESM2 and CanRCM4. Similarly, the northeast and central east also show narrow CIs and robust detection. An ALL signal is detected in six (CanRCM4), three (CanESM2), and four (CESM1) of the nine regions, demonstrating that detection for precipitation extremes is feasible (at least in certain regions) at smaller regional scales.

Using geopolitical regions, the ALL signal is detected for Canada in Rx1day and Rx5day with all three models and for the United States in Rx1day with CESM1 (*SI Appendix*, Fig. S4). Attribution occurs for Rx1day and Rx5day in Canada with the Canadian models and in Rx1day in the United States with CESM1. The US region covers most of the domain, minus the north; thus the results are slightly weaker than those for the North American mean in Fig. 2. Identifying a change from among the interannual variability may be easier in Canada, because the percentage increase in precipitation is expected to be larger in the higher latitudes due to enhanced warming and smaller variability because of generally smaller extreme values.

Extreme Event Attribution

For event attribution (24), we define extreme events based on the region mean PI. As the PI is computed locally at the grid box level, events of extreme mean PI values represent elevated total risk of local storms across the region, rather than precipitation averaged over the region. This is relevant for adaptation planning and emergency preparedness, as it is the compound occurrence of local extremes that can result in extreme high regional PI and increase the demands of regional response systems and adaptive capacity.

We focus on CanESM2 for this analysis so that we can compare ALL and NAT forcing. We determined the value of the 20-, 50-, and 100-y events for regional mean PI under historical NAT forcing, and then calculated the return periods of these events for current and future levels of global mean surface air temperature (GSAT) increase (see *Materials and Methods*) under ALL. The current climate has warmed about +1 °C compared with the preindustrial period, based on observations (35). The results are shown in Fig. 4 for Rx1day and in *SI Appendix*, Fig. S5 for Rx5day.

Most regions exhibit large reductions in return periods of extreme events with +1 °C of warming. The larger regions often show less uncertainty around the return period estimates, consistent with reductions in variability when averaging over larger spatial scales. For precipitation extremes, the spatial scale can have a large impact on event attribution results (20). The North American mean shows dramatic reductions in return periods. For example, a one in 20-y event in NAT becomes a one in 5-y event with +1 °C warming (relative to a preindustrial climate), while a one in 50-y (100-y) event becomes a one in 10-y (20-y) event. The 20-, 50-, and 100-y events are expected to occur about every 1.5 y to 2.5 y, on average, with +3 °C of warming. A decrease in return period (increase in probability) with ALL compared to NAT indicates that anthropogenic forcing will increase the likelihood of extreme precipitation events.

The smaller regions with large changes in likelihood (northeast, central east, southeast, and central west) showed strong increasing trends (*SI Appendix*, Table S1). Individual regions that demonstrated robust consistency between the temporal evolution of the model response and observations (Fig. 3) all show large reductions in extreme event return periods. However, even regions where a change is not detected over the historical period often exhibit increases in the likelihood of extreme region-level events (with +1 °C). Similar results are found for Rx5day (*SI Appendix*, Fig. S5), although the increases in likelihood are often smaller than those for Rx1day.

Discussion and Conclusions

We demonstrated an intensification of precipitation extremes over North America, with a contribution from human activity, using consistent results from different models, different methods, and physical understanding. The intensification of extreme precipitation and resulting increase in the likelihood of extreme events are expected to continue with additional warming.

Positive trends are found for the observed mean PI at the continental scale and for many regions. There is also a high likelihood of positive trends within the model ensembles. Positive trends are consistent with the expectation that extreme precipitation will increase due to increasing atmospheric humidity,

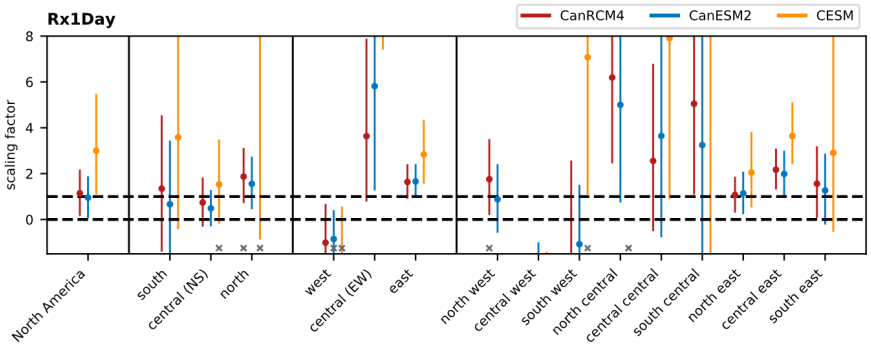

Fig. 3. As in Fig. 2 but for temporal regressions for individual regions.

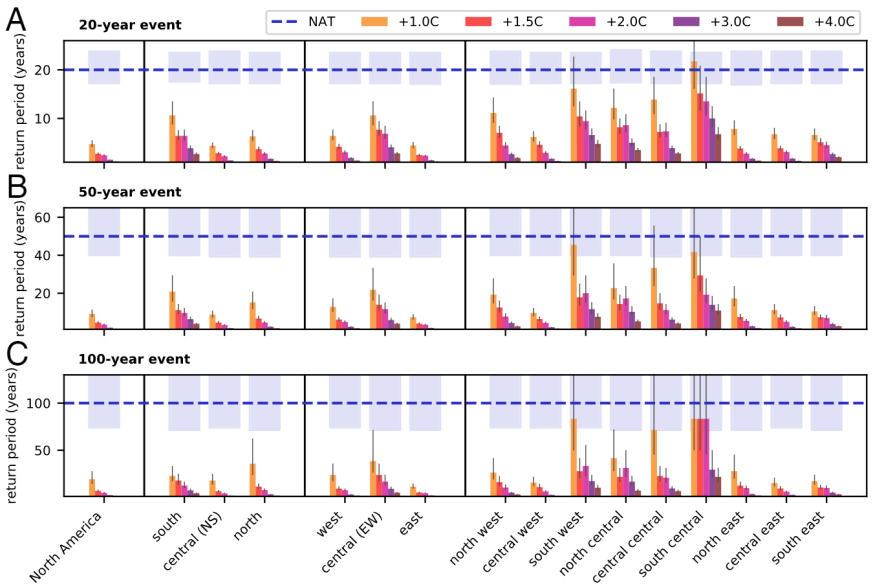

Fig. 4. Return periods for Rx1day 20-y (*A*), 50-y (*B*), and 100-y (*C*) events using CanESM2. For each region, event thresholds are defined from the natural-only simulations, and return periods for these events under different levels of GSAT increase in degrees Celsius relative to preindustrial are shown by colored bars. An increase of +1 °C represents the current climate. Error bars (and shading) indicate the 90% range. Note that different events use different vertical axis scales, and some ranges continue beyond the upper limit of the plot.

which increases proportionally to the temperature increase. Larger trends in the Canadian models are likely explained by stronger warming trends. Averaged over the North American domain, annual mean temperature anomalies in CanESM2 warm 1.77 °C over 1961–2010 based on a linear trend, while CESM1 warms 1.08 °C. Our result is consistent with a study involving tropospheric temperature (26), which found larger warming in the CanESM2 than in the CESM1 large ensemble. CanESM2 overestimates surface warming compared to observations (36).

A signal of combined anthropogenic and natural external forcing can be detected in the intensification of extreme precipitation at the continental scale over North America. In some cases, this intensification can be attributed to human influence specifically. All models agree that the ALL signal is detected; the differences in scaling factors between model families (Can vs. CESM1) are consistent with the trend differences. The detection results are considered robust due to consistency across the model ensembles, and are in agreement with the likelihood of positive trends.

An increase in the probability of extreme regional PI values is also attributed to human influence. Many regions already show an increase in the probability of modeled 20-, 50-, and 100-y region-level events, with greater increases at higher levels of global warming. Even regions that do not exhibit a detectable signal in the current climate show robust increases in the likelihood of extreme precipitation events with future warming. Strong increases in the likelihood of extreme regional PI values, especially with larger GSAT increases, are consistent with increasing trends and the detection of an ALL signal.

Performing the same detailed analyses with CanESM2 and the much higher-resolution CanRCM4, and finding close agreement, allows us to verify that the global climate model can provide robust information on regional precipitation changes. However, a required condition is that the model values are standardized appropriately (e.g., through the use of the PI). As we often do not have enough information to robustly estimate past and future changes in extreme precipitation at local scales (23), robust assessment of changes at larger spatial scales can be a useful alternative to guide local climate change adaptation.

Materials and Methods

Data and Processing. We use three initial-condition large ensembles of model simulations. CanESM2 (28) was used to produce a 50-member ensemble at a resolution of 2.8°. Historical forcing from the fifth phase of the Coupled Model Intercomparison Project was used for 1950–2005, and RCP8.5 was used for 2006–2100. For a large ensemble with CanRCM4 (29), each of 50 realizations was driven by a different realization from the CanESM2 ensemble. By design, consistent parameterizations were used for both models (29). CanRCM4 used the 50-km rotated-pole grid of the North American Coordinated Regional Climate Downscaling Experiment (37). The data are available at https://open.canada.ca/data/en/dataset/aa7b6823-fd1e-49ff-a6fb-68076a4a477c (CanESM2) and https://open.canada.ca/data/en/dataset/83aa1b18-6616-405e-9bce-af7ef8c2031c (CanRCM4). A large ensemble of the Community Earth System Model version 1 (CESM1) (30) has 40 realizations on a 1° grid with data from 1920–2100. As with CanESM2, RCP8.5 is used starting in 2006. We use daily precipitation from all models to calculate the chosen extremes indices with ref. 38.

HadEX2 (31) is a global gridded product derived from extremes indices calculated from station data. HadEX2 is presented on a 2.5° by 3.75° grid, with data coverage from 1901–2010. The extremes indices were calculated at the station level before an interpolation algorithm was applied.

The annual maxima were standardized by calculating a PI following refs. 11 and 12. For each grid box, annual maxima from 1979–2010 were fit to a stationary GEV distribution; a bootstrap goodness-of-fit test confirms the validity of this approach. Then, to determine the PI, each year was assigned the quantile of this GEV distribution that corresponds to its maximum precipitation value. The resulting PIs show little sensitivity to the base period used for fitting the distribution. For the NAT CanESM2 realizations, the PI was calculated using the GEV fit from the corresponding ALL realization.

In order to consider the impact of model resolution on the attribution results, time series of the PI were calculated for each grid box before the model values were interpolated to the standard HadEX2 grid. Regional averages were calculated using grid box area weights. Anomalies of the regional mean PI were calculated by subtracting the expected mean of 0.5, as in ref. 11.

Attribution of the Spatiotemporal Evolution. We utilize the Regularized Optimal Fingerprinting (ROF) method of ref. 39 to regress observations onto the model-simulated response. The use of the ROF method, in particular with the CanESM2 large ensemble, is discussed in more detail in ref. 27. In

general, the observations y are composed of the true climate response to all forcings y^* plus the influence of internal variability ϵ_0. The model response to each forcing x_i can similarly be represented by the forced response x^* plus the combined influence of internal variability and finite ensembles ϵ_i. A total least squares regression of the observations onto the model response results in scaling factors β,

$$y = y^* + \epsilon_0 \qquad x_i = x^* + \epsilon_i \qquad y^* = \sum_{i=1}^{m} \beta_i x_i^*,$$

that describe the relationship between the observations and the model-simulated response to a specific forcing.

An estimate of climate variability was determined from the difference between each model realization and the ensemble mean, which results in the number of estimates being one less than the ensemble size. We doubled the sample using ensemble mean differences from NAT simulations for CanESM2 and separately standardized future periods for CanRCM4 and CESM1. Separately for each model, half of each set of climate noise series were combined to calculate a covariance matrix that was regularized for prewhitening following ref. 39. The remaining series were used for a residual consistency test (40) and estimation of the CIs. Regional mean PI time series for 1961–2010 were used, with nonoverlapping 5-y means. The use of 5-y means is a common compromise between capturing shorter-scale features and keeping the estimated covariance matrix at a reasonable size. For the two-signal analysis, a regression was fit using model responses to ALL and NAT forcings, and the scaling factor for anthropogenic forcing was derived assuming a linear combination.

Extreme Event Attribution. To calculate the probabilities, the ensemble of annual values for a designated decade was used to calculate the probability of exceeding a certain threshold based on the percentage of values that exceed that threshold. The thresholds for extreme events are the 20-, 50-, and 100-y events as determined at each grid box using the NAT ensemble from 1981–2020. The return period was calculated as the reciprocal of the exceedance probability. A bootstrap procedure where individual years/members were resampled with replacement from the ensemble from a 10-y period provided the nonparametric 90% range.

The GSAT increase was calculated using GSAT from CanESM2 in 10-y periods relative to a mean from preindustrial control simulations. Decades where this increase was $+1.0\ ^\circ$C, $+1.5\ ^\circ$C, $+2.0\ ^\circ$C, etc., were selected for analysis.

ACKNOWLEDGMENTS. We thank the modeling groups for producing the large ensemble simulations, and John Fyfe, Nathan Gillett, and three anonymous reviewers for valuable comments on this manuscript.

1. U. Lall *et al.*, "Water" in *Impacts, Risks, and Adaptation in the United States: Fourth National ClimateAssessment,* D. R. Reidmiller *et al.*, Eds. (US Global Change Research Program, Washington, DC, 2018), vol. II, pp. 145–173.
2. R. Story *et al.*, "Estimate of the average annual cost for disaster financial assistance arrangements due to weather events" (Office of the Parliamentary Budget Officer, Ottawa, Canada, 2016).
3. D. R. Easterling *et al.*, "Precipitation change in the United States" in *Climate Science Special Report: Fourth National Climate Assessment,* D. J. Wuebbles *et al.*, Eds. (US Global Change Research Program, Washington, DC, 2017), vol. I, pp. 207–230.
4. B. Teufel *et al.*, Investigation of the 2013 Alberta flood from weather and climate perspectives. *Clim. Dynam.* **48**, 2881–2899 (2017).
5. K. van der Wiel *et al.*, Rapid attribution of the August 2016 flood-inducing extreme precipitation in south Louisiana to climate change. *Hydrol. Earth Syst. Sci.* **21**, 897–921 (2017).
6. C. M. Patricola, M. F. Wehner, Anthropogenic influences on major tropical cyclone events. *Nature* **563**, 339–346 (2018).
7. X. Zhang *et al.*, Detection of human influence on twentieth-century precipitation trends. *Nature* **448**, 461–465 (2007).
8. K. Marvel, C. Bonfils, Identifying external influences on global precipitation. *Proc. Natl. Acad. Sci. U.S.A.* **110**, 19301–19306 (2013).
9. D. Polson, G. C. Hegerl, X. Zhang, T. J. Osborn, Causes of robust seasonal land precipitation changes. *J. Clim.* **26**, 6679–6697 (2013).
10. H. Wan, X. Zhang, F. Zwiers, S.-K. Min, Attributing northern high-latitude precipitation change over the period 1966–2005 to human influence. *Clim. Dynam.* **45**, 1713–1726 (2015).
11. X. Zhang, H. Wan, F. W. Zwiers, G. C. Hegerl, S.-K. Min, Attributing intensification of precipitation extremes to human influence. *Geophys. Res. Lett.* **40**, 5252–5257 (2013).
12. S.-K. Min, X. Zhang, F. W. Zwiers, G. C. Hegerl, Human contribution to more-intense precipitation extremes. *Nature* **470**, 378–381 (2011).
13. B. B. Sarojini, P. A. Stott, E. Black, Detection and attribution of human influence on regional precipitation. *Nat. Clim. Change* **6**, 669–675 (2016).
14. J.-L. Martel, A. Mailhot, F. Brissette, D. Caya, Role of natural climate variability in the detection of anthropogenic climate change signal for mean and extreme precipitation at local and regional scales. *J. Clim.* **31**, 4241–4263 (2018).
15. J. M. Eden *et al.*, Extreme precipitation in The Netherlands: An event attribution case study. *Weather Clim. Extrem.* **21**, 90–101 (2018).
16. L. N. Luu, R. Vautard, P. Yiou, G. J. van Oldenborgh, G. Lenderink, Attribution of extreme rainfall events in the South of France using EURO-CORDEX simulations. *Geophys. Res. Lett.* **45**, 6242–6250 (2018).
17. A. D. King *et al.*, Limited evidence of anthropogenic influence on the 2011-12 extreme rainfall over southeast Australia. *Bull. Am. Meteorol. Soc.* **94**, S55–S58 (2013).
18. G. J. van Oldenborgh, F. E. L. Otto, K. Haustein, K. AchutaRao, The heavy precipitation event of December 2015 in Chennai, India. *Bull. Am. Meteorol. Soc.* **97**, S87–S91 (2016).
19. N. Schaller et al., The heavy precipitation event of May–June 2013 in the upper Danube and Elbe basins. *Bull. Am. Meteorol. Soc.* **95**, S69–S72 (2014).
20. M. C. Kirchmeier-Young, H. Wan, X. Zhang, S. I. Seneviratne, Importance of framing for extreme event attribution: The role of spatial and temporal scales. *Earth's Future* **7**, 1192–1204 (2019).
21. E. M. Fischer, R. Knutti, Anthropogenic contribution to global occurrence of heavy-precipitation and high-temperature extremes. *Nat. Clim. Change* **5**, 560–564 (2015).
22. N. Maher *et al.*, The Max Planck Institute Grand ensemble: Enabling the exploration of climate system variability. *J. Adv. Model. Earth Syst.* **11**, 2050–2069 (2019).
23. C. Li, F. Zwiers, X. Zhang, G. Li, How much information is required to well-constrain local estimates of future precipitation extremes? *Earth's Future* **7**, 11–24 (2019).
24. National Academies of Science Engineering and Medicine, *Attribution of Extreme Weather Events in the Context of Climate Change* (The National Academies Press, Washington, DC, 2016).
25. N. Massey et al., Weather@Home—Development and validation of a very large ensemble modelling system for probabilistic event attribution. *Q. J. R. Meteorol. Soc.* **141**, 1528–1545 (2015).
26. B. D. Santer *et al.*, Quantifying stochastic uncertainty in detection time of human-caused climate signals. *Proc. Natl. Acad. Sci. U.S.A.* **116**, 19821–19827 (2019).
27. M. C. Kirchmeier-Young, F. W. Zwiers, N. P. Gillett, Attribution of extreme events in Arctic sea ice extent. *J. Clim.* **30**, 553–571 (2017).
28. V. K. Arora *et al.*, Carbon emission limits required to satisfy future representative concentration pathways of greenhouse gases. *Geophys. Res. Lett.* **38**, L05805 (2011).
29. J. F. Scinocca *et al.*, Coordinated global and regional climate modeling. *J. Clim.* **29**, 17–35 (2016).
30. J. E. Kay *et al.*, The Community Earth System Model (CESM) Large Ensemble Project. *Bull. Am. Meteorol. Soc.* **96**, 1333–1349 (2015).
31. M. G. Donat *et al.*, Updated analyses of temperature and precipitation extreme indices since the beginning of the twentieth century: The HadEX2 dataset. *J. Geophys. Res. Atmos.* **118**, 2098–2118 (2013).
32. T. DelSole, L. Trenary, X. Yan, M. K. Tippett, Confidence intervals in optimal fingerprinting. *Clim. Dynam.* **52**, 4111–4126 (2019).
33. F. Lehner, A. P. Schurer, G. C. Hegerl, C. Deser, T. L. Frölicher, The importance of ENSO phase during volcanic eruptions for detection and attribution. *Geophys. Res. Lett.* **43**, 2851–2858 (2016).
34. B. D. Santer et al., Volcanic contribution to decadal changes in tropospheric temperature. *Nat. Geosci.* **7**, 185–189 (2014).
35. M. R. Allen *et al.*, "Framing and Context" in *Global Warming of 1.5 °C. An IPCC Special Report on the Impacts of Global Warming of 1.5 °C above Pre-industrial Levels and Related Global Greenhouse Gas Emission Pathways, in the Context of Strengthening the Global Response to the Threat of Climate Change*, V. Masson-Delmotte *et al.*, Eds. (Intergovernmental Panel on Climate Change, 2018), in press.
36. J. Sheffield *et al.*, North American climate in CMIP5 experiments. Part I: Evaluation of historical simulations of continental and regional climatology. *J. Clim.* **26**, 9209–9245 (2013).
37. F. Giorgi, C. Jones, G. R. Asrar, Addressing climate information needs at the regional level: The CORDEX framework. *World Meteorol. Organ. Bull.* **58**, 175–183 (2009).
38. U. Schulzweida, *CDO User Guide*, (Max Planck Institute for Meteorology, 2019).
39. A. Ribes, S. Planton, L. Terray, Application of regularised optimal fingerprinting to attribution. Part I: Method, properties and idealised analysis. *Clim. Dynam.* **41**, 2817–2836 (2013).
40. S. F. B. Tett, P. A. Stott, M. R. Allen, W. J. Ingram, J. F. B. Mitchell, Causes of twentieth-century temperature change near the Earth's surface. *Nature* **399**, 569–572 (1999).